Light-induced water oxidation at silicon electrodes functionalized with a cobalt oxygen-evolving catalyst

Joep J. H. Pijpers[a,b], Mark T. Winkler[c], Yogesh Surendranath[a], Tonio Buonassisi[c], and Daniel G. Nocera[a,1]

[a]Department of Chemistry; and [c]Department of Mechanical Engineering, Massachusetts Institute of Technology, Cambridge, MA 02139-4307; and [b]Foundation for Fundamental Research on Matter (FOM) Institute for Atomic and Molecular Physics, Science Park 104, 1098 XG, Amsterdam, The Netherlands

Contributed by Daniel G. Nocera, April 30, 2011 (sent for review March 30, 2011)

Integrating a silicon solar cell with a recently developed cobalt-based water-splitting catalyst (Co-Pi) yields a robust, monolithic, photo-assisted anode for the solar fuels process of water splitting to O_2 at neutral pH. Deposition of the Co-Pi catalyst on the Indium Tin Oxide (ITO)-passivated *p*-side of a *np*-Si junction enables the majority of the voltage generated by the solar cell to be utilized for driving the water-splitting reaction. Operation under neutral pH conditions fosters enhanced stability of the anode as compared to operation under alkaline conditions (pH 14) for which long-term stability is much more problematic. This demonstration of a simple, robust construct for photo-assisted water splitting is an important step towards the development of inexpensive direct solar-to-fuel energy conversion technologies.

photoelectrochemical | hydrogen | solar energy | storage

Photosynthetic organisms convert the energy of sunlight into chemical energy by splitting water, producing molecular oxygen and hydrogen equivalents in the highly conserved enzyme complex photosystem II (PSII) (1). Absorbed photons are transferred to the reaction center of PSII, where a single electron/hole charge separation occurs. The oxidative power of the photo-produced hole in PSII is transferred to the oxygen evolving complex (OEC) where water splitting occurs. The electron is transferred to the adjacent photosystem I (PSI), where it participates in the reduction reaction of NAD^+ into NADH, which is ultimately used to fix CO_2. Crucial in the above configuration is the separation of the functions of light collection and conversion from catalysis. Whereas light collection/conversion generates electron/hole pairs one at a time, water splitting is a four-electron/hole process (2, 3). Hence, the multielectron catalysts of PSII and PSI, positioned at the terminus of the photosynthetic charge-separating network, are compulsory so that the one photon-one-electron/hole "wireless current" can be bridged to the four-electron/hole chemistry of water splitting.

An artificial photosynthesis can be designed if the one-electron/hole wireless current of a semiconductor can be integrated directly with catalysts to perform the four-electron-four proton catalysis of water splitting. To this end, an important recent advance has been the creation of a cobalt-phosphate (Co-Pi) catalyst (4, 5) that captures the functional elements of the OEC of PSII (6). As in PSII OEC, the Co-Pi catalyst self-assembles upon oxidation of an earth-abundant metal [Co^{2+} for Co-Pi vs. Mn^{2+} for OEC (7–9)] in phosphate-buffered solutions at neutral pH (4, 10), exhibits high activity in natural water and sea water at room temperature (11), activates water by proton-coupled electron transfer (3) [as does the OEC of PSII (12, 13)], and is self-healing (14) [as is PSII (15–18)]. Moreover, X-ray Absorption Spectroscopy (XAS) studies (19, 20) have established that the Co-Pi catalyst is a structural relative of PSII OEC. PSII OEC is a Mn_3CaO_4-Mn cubane (21) where the fourth Mn atom is linked via a μ-oxo-bridge. The predominate structure of Co-Pi in *ca.* nanometer thin films is a Co_3AO_4-Co (A = alkali metal ion) biscubane that is the head-to-tail dimer of PSII OEC.

The Co-Pi catalyst may be interfaced to semiconducting metal-oxides to enhance the efficiency of photoelectrochemical water splitting. In particular, Co-Pi has been deposited onto Fe_2O_3 (22–24), and WO_3 thin films (25) and on ZnO rods (26) to effect a several hundred-millivolt reduction in the onset potential for water oxidation relative to the unfunctionalized photoanode. For Fe_2O_3 (23) and WO_3 (25) films, this promising reduction of the onset potential has been achieved at neutral pH. While these metal-oxide semiconductors benefit from high photoelectrochemical stability, their large band-gaps and losses associated with bulk and interfacial transport place limits on the theoretical efficiency of overall water splitting (27). Among nonoxides, silicon (Si) is a preferred semiconductor material because it absorbs a significant part of the solar spectrum, is earth-abundant, has low losses associated with bulk and interfacial carrier transport, and hence it is widely used in photovoltaic applications. The integration of *np*-Si junctions with water splitting has the potential to significantly reduce current costs of solar energy conversion by potentially reducing the balance of system costs attendant to separate devices for solar capture/conversion and storage (28–30). Such an approach is particularly well suited for small-scale solar-to-fuel devices, which have enormous potential for decentralized power generation and storage, particularly in developing economies (31).

The realization of Si-based, direct solar-to-fuel devices hinges on overcoming the inherent photoelectrochemical instability of Si in the presence of the highly oxidizing conditions of water splitting (32, 33). We now show that Si surfaces can be effectively protected from photoinstability at neutral pH with thin layers of Indium Tin Oxide (ITO) and that the passivated *np*-Si junction can function as efficient photoassisted anodes for the water oxidation when integrated with the Co-Pi catalyst. Photogenerated electrons and holes are separated within the *np*-Si junction, analogous to the wireless current in natural photosynthesis. Holes migrate to the ITO-contacted *p*-side of the Si cell to drive the water oxidation reaction mediated by Co-Pi. Nearly all the voltage generated in the buried *np*-Si junction is delivered to the catalyst layer effecting a significant light-induced reduction of the onset potential for water splitting. The realization of Co-Pi-functionalized passivated *np*-Si junctions opens the prospect of designing integrated devices (e.g., artificial leaf) for direct solar-to-fuels conversion.

Results and Discussion

A schematic representation of the illuminated Co-Pi-functionalized *np*-Si electrode and its energy diagrams in dark and under illumination (for water oxidation at 1 mA/cm^2) are given in

Author contributions: J.J.H.P., M.T.W., Y.S., T.B., and D.G.N. designed research; J.J.H.P., M.T.W., and Y.S. performed research; J.J.H.P. contributed new reagents/analytic tools; J.J.H.P., M.T.W., Y.S., and T.B. analyzed data; and J.J.H.P. and D.G.N. wrote the paper.

The authors declare no conflict of interest.

[1]To whom correspondence should be addressed. E-mail: nocera@mit.edu.

This article contains supporting information online at www.pnas.org/lookup/suppl/doi:10.1073/pnas.1106545108/-/DCSupplemental.

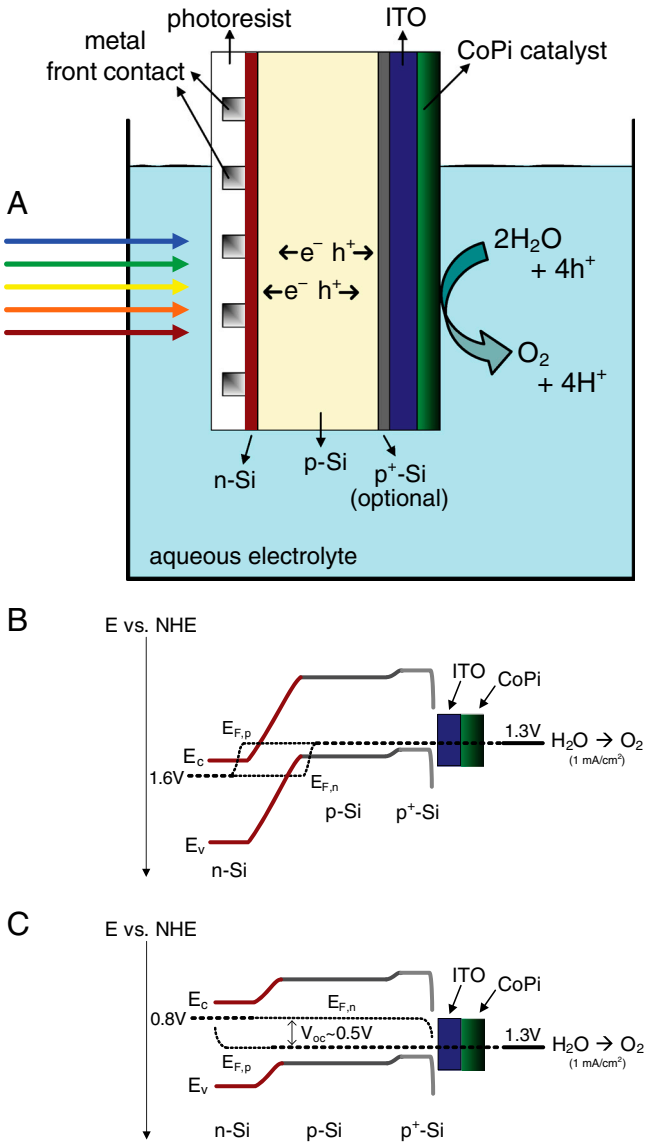

Fig. 1. (*A*) Schematic of a Co-Pi-functionalized *npp*$^+$-Si junction and its energy diagram in the situation of an anodic current of 1 mA/cm^2 (requiring a potential of 1.3 V vs. NHE at the ITO|CoPi interface) for the dark (*B*) and under illumination (*C*), labeled with conduction band (E_C), valence band (E_V) and quasi-Fermi energy levels for holes and electrons ($E_{F,p}$ and $E_{F,n}$, respectively).

Fig. 1. All films, excepting the Co-Pi film, were deposited by Radio Frequency (RF) or Direct Current (DC) sputtering. Prior to the first sputtering deposition, the native oxide layer was removed by dipping *np*-Si in a Hydrofluoric Acid (HF)-solution (~10 wt%). In some of the samples, a p^+ layer was incorporated by depositing a 1 μm film of Si-doped (1%) Al on the *p*-side of the junction, followed by a rapid thermal annealing step in N_2 at 900 °C (34). An interfacial SiO_2 (~1.5 nm) layer was intentionally deposited on the *p*-side of the junction to provide a smooth transition from the Si substrate to the overlying passivating layer (35) so that recombination caused by high interface state densities due to mismatch in lattice constants, expansion coefficients, and other geometric factors is minimized. Because water molecules can penetrate into the Co-Pi film (3, 11), the catalyst cannot be directly deposited on the *p*-side of the *np*-Si junction, since Si at the interface would quickly oxidize into a thick SiO_2 layer (35), which is an effective barrier for charge transfer. Therefore, a 50-nm film of ITO was deposited on the *p*-side of the Si junction as a protective barrier layer. Samples were annealed (400 °C, N_2, 30 min) to enhance the conducting properties of the ITO (36). A patterned metal front contact (Ti/Pd/Ag, 20/20/100 nm thickness, respectively) was deposited on the *n*-side of the sample. On top of this contact, a 10-μm layer of photoresist (AZ Electronic Materials, AZ-9260) was spin-cast to prevent the metal and *n*-Si surfaces from contacting water when the sample was immersed in the electrolyte. Finally, the Co-Pi film was grown on top of the ITO layer by means of electrodeposition (*SI Appendix: Fig. S1*). In a typical photoelectrochemical experiment (vide infra), a sample of Co-Pi-functionalized *np*-Si is immersed in an aqueous 0.1 M potassium phosphate (KPi) electrolyte and illuminated from the *n*-side. Absorption of light by the photoresist is negligible, as can been concluded from the absorption spectrum of the photoresist (*SI Appendix: Fig. S2*).

Fig. 2 shows a comparison of the cyclic voltammograms (CV) of *np*Si|ITO|Co-Pi and *npp*$^+$Si|ITO|Co-Pi anodes. In both cases, a film of the Co-Pi catalyst (250 nanomole Co) was electrodeposited (see *SI Appendix*). In principle, the Co-Pi catalytic activity can be increased by using thicker films (>7,500 nanomoles), but transport limitations within thick films cause deviations in the current-voltage behavior (3). The sample was immersed in a 0.1 M KPi electrolyte at pH 7. Under these conditions, the Nernstian potential for water oxidation is 0.82 V vs. a normal hydrogen electrode (NHE). When applying the potential through the ITO thin film in the dark (Fig. 2, blue trace), the onset for water oxidation occurs at 1.2 V vs. NHE, implying an overpotential of ~0.4 V. This value is in agreement with the required overpotential for Co-Pi on commercial ITO electrodes (3, 4). The significant currents in this electrode configuration, in which the photovoltaic (PV) component is shorted, indicate that the sputtered ITO film has a sufficiently low sheet resistance (170 Ω/sq, as determined in a four-point probe measurement). The onset for water oxidation remains located at 1.2 V, but the observed dark currents are much lower (Fig. 2, black trace) when the potential is applied through the metal contacts, such that current must flow through the PV component. Under reverse-bias conditions for the *np*-Si junction (e.g., positive applied potentials), the dark anodic current is determined by the leakage current across the *np*-Si junction, which should be negligible for a highly quality *np*-Si junction. The low but nonnegligible dark

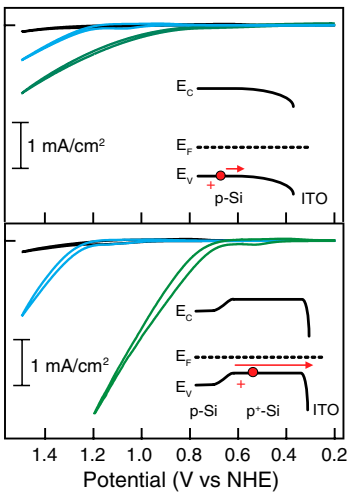

Fig. 2. CV curves of Si|ITO|Co-Pi samples (Top) without and (Bottom) with the p^+-layer. The samples were immersed in a 0.1 M KPi electrolyte in dark (black line) and illuminated with a Xe lamp (green line, intensity ~100 mW/cm^2). The scan rate was 2.5 mV/s. The thickness of the Co-Pi film was ~36 nm. The powder blue curves correspond to the dark CV curve when the potential was applied through the ITO film at the back. The insets show the energy diagrams at the Si|ITO interface, labeled with conduction band (E_C), valence band (E_V) and Fermi (E_F) energy levels.

current from our *np*-Si junctions (Fig. 2) reveals that the solar cell is partially shunted.

When illuminating the structure from the *n*-side with 100 mW/cm^2 light from a Xe lamp (AM1.5 illumination), the potential onset for water oxidation is decreased significantly for both the *np*Si|ITO|Co-Pi and the *npp*$^+$Si|ITO|Co-Pi sample (Fig. 2). Clearly, photogenerated holes in the Si are injected into the ITO film, after which they participate in the water oxidation reaction at the Co-Pi catalyst. As can be seen in *SI Appendix: Fig. S4*, incorporation of the Co-Pi catalyst results in a much lower onset potential for water oxidation (both in light and dark) compared to Si|ITO electrodes without Co-Pi, illustrating the benefit of functionalizing passivated *np*-Si junctions with the Co-Pi catalyst.

The current increases much faster with potential for the *npp*$^+$Si|ITO|Co-Pi sample than for the *np*Si|ITO|Co-Pi sample even though photoexcited carriers presumably encounter the same, negligible series resistance in the bulk of either device (under illumination). These disparate CV characteristics can be explained by considering the non-Ohmic nature of the *p*Si|ITO interface compared to that of the p^+Si|ITO interface. When *p*-Si is brought in contact with ITO, equilibration of the Fermi levels is achieved by exchange of charge carriers across the interface. Because the work function of ITO [4.4–4.7 eV (37, 38)] is smaller than that of *p*-Si [5.0–5.2 eV (39)], electrons will flow from the ITO into the *p*-Si, creating a negatively charged space-charge layer in the Si with associated downward band bending (Fig. 2, inset). The negative charge acquired accumulates mainly at fixed acceptor impurity atoms. In the relatively lightly doped *p*-Si, the space-charge region can extend far into the *p*-Si (up to ~1 μm) and the resulting downward band bending acts as a Schottky barrier for hole transport. In the highly doped p^+-layer, in contrast, the space-charge region extends only a few nanometers into the p^+-layer because of the high number of dopant atoms that can accept the electrons from the ITO (Fig. 2, inset). Hence, the space-charge region in the p^+ layer is thin enough for holes to tunnel across the p^+-Si|ITO interface, which behaves as an Ohmic contact.

A prefeature prior to the catalytic wave is observed in the CVs of Fig. 2 for anodes in the dark and under illumination. This prefeature is attributed to oxidation of Co^{2+} centers in the Co-Pi film to Co^{3+} and, partially, Co^{4+} centers (3, 40, 41); these redox conversion processes give rise to transient currents. Upon prolonged electrolysis at the "prefeature potential," the current decreases to zero, indicating that negligible residual water oxidation catalysis takes place at the prefeature potential.

The energy band diagrams corresponding to steady-state operation in dark and under illumination at 1 mA/cm^2 current are given in Fig. 1 *B* and *C*, respectively, for an *npp*$^+$Si|ITO|Co-Pi anode. Previous reports (3, 4, 10) as well as steady-state data obtained here (vide infra) establish that ~1.3 V vs. NHE is required to maintain a 1 mA/cm^2 current density for water oxidation on a 2D surface, thus pinning the potential at the ITO|Co-Pi solution interface at ~1.3 V. Because the rectifying characteristics of the *np*-Si junction impede anodic current flow, a larger reverse-bias of ~1.6 V vs. NHE must be applied to the anode in the dark to enable 1 mA/cm^2 of anodic current to tunnel across the buried *np*-Si junction (Fig. 1*B*). In contrast, a much lower potential of 0.8 V vs. NHE is needed to attain a 1 mA/cm^2 current density under illumination (Fig. 1*C*). This reduction of the required applied potential originates both from the photovoltage generated by the solar cell (0.5 V) and from the lower impedance of the *np*-Si junction under illumination because excited photocarriers can move freely through the conduction and valence bands. The foregoing discussion highlights a key distinction between this construct and a conventional photoelectrochemical anode. In the latter, photovoltage generation and current rectification occur at the solution/semiconductor interface. The driving force for water oxidation is therefore dictated by the energy of the band edge relative to the thermodynamic potential for water oxidation. In the construct of Fig. 1, the photovoltage generation and current rectification occur at the buried *np*-Si junction. Thus, it is the intersection of the *i*-V curve of the PV component with the *i*-V curve of the Co-Pi electrochemical component that dictates the (photo)potential and (photo) current available for water splitting (42).

Further insight in the presence of non-Ohmic interfaces within the Si|ITO|Co-Pi structures is provided by examining the Tafel behavior (43). For the native catalyst on ITO, a Tafel slope near 59 mV/decade is characteristic of an O_2 evolution mechanism involving a reversible one-electron transfer prior to a chemical turnover-limiting step (3). For the experiments described here, mechanistic information about the Co-Pi catalyst from the Tafel plot is convoluted by the electrical properties of the PV and ITO components of the anode. Accordingly, the Tafel data is examined solely as a measure of the steady-state activity of the photo-assisted anode as a function of applied potential. For the *np*Si|ITO|Co-Pi in Fig. 3*A*, the slope of the Tafel plot is 285 mV/decade when measured in the dark and 275 mV/decade when measured under 100 mW/cm^2 illumination. We attribute the large values of the Tafel slopes to the non-Ohmic contact at the *p*Si|ITO interface. For the *npp*$^+$Si|ITO|Co-Pi (Fig. 3*B*) in the dark, the slope of the Tafel plot is also large (220 mV/decade), which is consistent with the high impedance for anodic current across the reverse-biased *np*-Si junction in the dark. Under 100 mW/cm^2 illumination, however, the Tafel slope is reduced significantly to a value of 106 mV/decade indicative of greater carrier mobility through the Si conduction and valence bands and the more attractive Ohmic nature of the p^+Si|ITO interface. When applying the potential through the ITO film both for *np*Si|ITO|Co-Pi and for *npp*$^+$Si|ITO|Co-Pi samples, the Tafel slope is found to be 110 mV/decade. That this value is higher than the 59 mV/decade that was observed for Co-Pi on ITO electrodes (3, 10) implies hindered conduction across the sputtered 50 nm ITO film. The Tafel data in Fig. 3 underlines the importance of establishing an Ohmic contact at the *p*Si|ITO interface. Although the onset potential for water oxidation is significantly reduced when illuminating the *np*Si|ITO|Co-Pi sample, excessive overpotentials are nevertheless required to attain significant anodic currents, as evidenced from the higher Tafel slopes of Fig. 3*A*.

The reduction of the onset for water oxidation for the *npp*$^+$Si|ITO|Co-Pi sample can be accurately determined from the Tafel data in Fig. 3*B*. At low current densities (where the Tafel behavior is linear), the potential required for a given current density is reduced by ~0.52 V when the anode is subject to 100 mW/cm^2 illumination (~AM 1.5). Given the fact that the V_{oc} of the *npp*$^+$Si|ITO solar cell is 0.57 V under AM 1.5 illumination

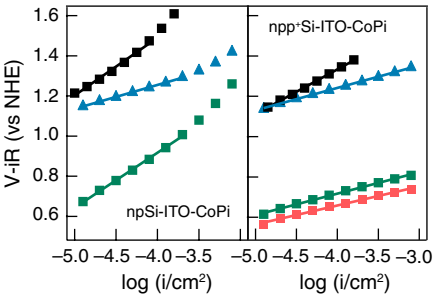

Fig. 3. Tafel plots for (Left) *np*Si|ITO|Co-Pi and (Right) *npp*$^+$Si|ITO|Co-Pi with potential applied to the metal front contact for measurements in dark (black squares), at 100 mW/cm^2 (green squares), and 1,000 mW/cm^2 (orange red squares) illumination. The blue triangles correspond to a measurement in dark where the potential was applied through the ITO film at the back of the sample.

(*SI Appendix: Fig. S3*), we conclude that most of the generated photopotential in the solar cell is utilized to reduce the onset potential for water oxidation.

The magnitude of the external potential required to attain a given current density is well described by the intrinsic properties of the solar cell, as is demonstrated in Fig. 4. In particular, the photovoltage, and, therefore, the necessary bias voltage, scales logarithmically with the light intensity in parallel with a corresponding increase in V_{oc} for the isolated solar cell (44). Fig. 4*A* shows the potential required to drive water oxidation at a constant current of 20 μA/cm^2 through an *npp*$^+$Si|ITO|Co-Pi photoanode as a function of the illumination intensity. The onset potential for water oxidation shifts to lower values for higher illumination intensities in line with the expected increase in V_{oc}. Fig. 4*A* also shows the results of the same galvanostatic experiment for an *np*Si|ITO|Co-Pi photoanode. Again, the onset potential for water oxidation is reduced for increasing illumination intensities. In the dark, a potential of 1.20 V is required to attain a current of 20 μA/cm^2 for the *npp*$^+$Si|ITO|Co-Pi sample whereas the required potential is 1.29 V for the *np*Si|ITO|Co-Pi sample. This discrepancy is ascribed to the non-Ohmic nature of the *p*Si|ITO interface, thus leading to a higher overpotential to attain a given anodic current.

Fig. 4*B* shows the incident-photon-to-current-efficiency (IPCE) as a function of wavelength for a *npp*$^+$Si|ITO solar cell (measured in air), a *npp*$^+$Si|ITO|Co-Pi sample, and a *np*Si|ITO|Co-Pi sample. The shape of these three data traces is very similar, implying that most of the anodic current originates from absorption of 600–900 nm photons. As in a regular Si solar cell, there are significant losses in the visible region (400–600 nm) and above 1,000 nm because of recombination in the emitter layer and recombination at the back surface, respectively (44). Additionally, light trapping was not optimized for the solar cells, leading to additional losses across the entire spectrum. Fig. 4*B* once more clearly illustrates the necessity of a good Ohmic contact at the *p*Si|ITO interface as carrier collection is very inefficient when this interface is non-Ohmic.

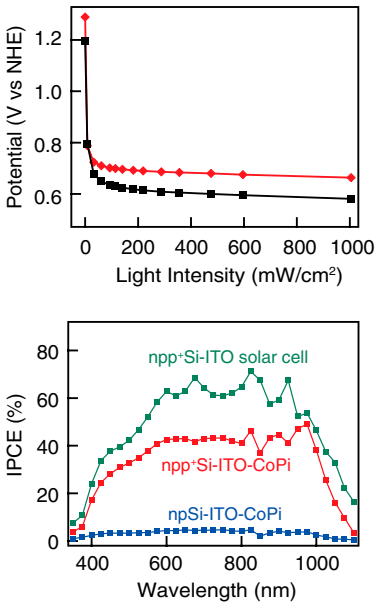

Fig. 4. (Top) Potential required to drive a galvanostatic current of 20 μA through an *np*Si|ITO|Co-Pi sample (red trace) and through an *npp*$^+$Si|ITO|Co-Pi sample (black trace) as a function of the illumination intensity. The lines are a guide to the eye. (Bottom) IPCE as a function of wavelength for a *npp*$^+$Si|ITO solar cell (green trace measured in air), for the *npp*$^+$Si|ITO|Co-Pi sample (red data) and for the *np*Si|ITO|Co-Pi sample (blue data).

The Faradaic efficiency of the Co-Pi-sensitized *np*-Si was measured with a fluorescence-based O_2 sensor. *SI Appendix: Fig. S5* shows that, after initiating electrolysis at 0.9 V vs. NHE, the percentage of O_2 detected in the headspace increased in accordance with attributing all current to result from the $4e^-$ oxidation of water to produce O_2. The O_2 detection experiment in *SI Appendix: Fig. S5* demonstrates that the photocurrent in the *np*-Si|ITO|Co-Pi samples is stable minimally over a period of 12 h in 0.1 M KPi electrolyte and that the Faradaic efficiency for O_2 production remains unity. Long-term stability of the device benefits from operation at pH 7. ITO is chemically unstable in acidic media (45) and the conductivity of ITO decreases upon anodization in basic electrolytes (46). That the functionalized electrode described here can operate at pH 7 is a distinct advantage over water-splitting concepts in more extreme pH conditions.

The foregoing results are obtained on Co-Pi-functionalized *single-junction* Si cells, for which the open circuit voltage (V_{oc}) falls in the expected 0.5–0.7 V range (44). Because this voltage is too low to supply the entire thermodynamic potential of 1.23 V, an applied external voltage was required. To perform water splitting without an external voltage bias, the Co-Pi catalyst must be integrated with a Si-based tandem cell of sufficient V_{oc} (47, 48) or alternatively, with two or more single-junction Si cells connected in series to provide a sufficient photopotential for water oxidation. In line with the latter possibility, a *npp*$^+$Si|ITO|Co-Pi photoanode was connected in series to an additional *npp*$^+$Si|ITO cell via alligator clips that were interconnected with copper wires. Good contact between the clips and the metal|ITO substrate was achieved by means of silver paint. Fig. 5 shows the CVs for a single *npp*$^+$Si|ITO|Co-Pi sample immersed in a 0.1 M KPi electrolyte in dark and under illumination with a Xe lamp (dark blue line, intensity ~100 mW/cm^2). Similar as in Fig. 2, illumination leads to a decrease of the potential onset for water oxidation by 0.5 V. Upon connecting the second solar cell in series with the *npp*$^+$Si|ITO|Co-Pi photoanode, the potential onset was further reduced by another 0.5 V.

The solar conversion efficiency for O_2 production was determined from:

$$\eta(\%) = \frac{100(E_{\text{Nernst}} - E_{\text{appl}})i}{P_{hv}A} \qquad [1]$$

in which E_{Nernst} is the Nernstian potential for water oxidation relative to NHE, E_{appl} is the applied potential relative to NHE, i is the current at a given applied potential, P_{hv} is the power density of the incident light, and A is the illuminated area. Eq. **1** deviates slightly from previous equations of this type (49) because our values of E_{appl} are derived from measurements made relative to a reference electrode. Thus, the efficiency metric η reflects an

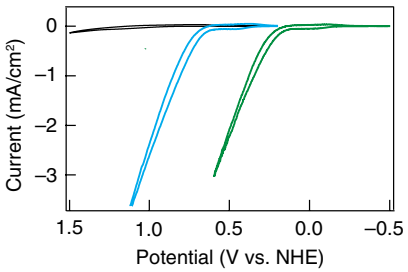

Fig. 5. IV curves of an *npp*$^+$Si|ITO|Co-Pi sample immersed in a 0.1 M KPi electrolyte in dark (black line) and under illumination with a Xe lamp (powder blue line). The IV curve of an *npp*$^+$Si|ITO|Co-Pi sample under illumination when connected to an additional solar cell (*npp*$^+$Si|ITO) in series (green line). The scan rate was 2.5 mV/s for all traces and the irradiation intensity corresponded to AM 1.5 illumination.

upper limit value expected for solar-to-hydrogen efficiency that ignores overpotential losses at the cathode and Ohmic resistive losses in the cell. We prefer to use Eq. **1** because it isolates the performance of the Co-Pi|Si photoanode. For a single npp^+Si|ITO|Co-Pi cell, the maximum measured value of η was 0.015% (measured over a potential range of ~300 mV from the onset potential under illumination). This low value of η arises because in a single cell configuration, only 0.5 V photopotential is available; the remaining potential is applied externally. Along this line, connecting a second solar cell in series leads to an increase in maximum efficiency to 0.25% since an additional 0.5 V is now derived from the photopotential, thereby reducing the externally applied potential. Higher values of η may be obtained by connecting a third solar cell in series, which will omit the need for applying an external potential and thus permit efficiencies in excess of the highest reported efficiency for a metal-oxide CoPi system (~0.25%) (23). We note that Si absorbs a larger fraction of incident solar irradiance than metal-oxide semiconductors due to its lower band gap, thus utilizing near-infrared photons that are not absorbed in metal-oxide semiconductors. Hence, our results are consistent with theoretical predictions (27) that multiphoton water-splitting configurations (in which the required potential is generated by sequential absorption of multiple photons) are more efficient than single-photon water splitting. The forgoing discussion highlights that the value of η as defined in Eq. **1**, when determined for a single half reaction of water splitting, can be an ambiguous metric, particularly when comparing light absorbers of disparate bandgaps (e.g., Si vs. Fe_2O_3).

An alternative efficiency metric, which is particularly relevant for the optimization of the electrochemical interface, is the percent of the maximum power generated by the photovoltaic component that is utilized to drive the electrochemical half reaction. This can be calculated as follows:

$$\eta(\%) = \frac{100 \cdot \Delta V \cdot i}{P_{hv} A \cdot \eta_{PV}} \qquad [2]$$

in which η_{PV} is the peak solar-to-electrical power conversion efficiency, determined from the I-V curve of an identically prepared solar cell (*SI Appendix: Fig. S3*), and ΔV is the potential difference between the light and the dark (connected to ITO) Tafel plots in Fig. 3. Using Eq. **2**, the efficiency is 5.6% for a single npp^+Si|ITO|Co-Pi electrode at an applied potential of 0.8 V vs. NHE. *SI Appendix: Fig. S6* gives a comparison of the two calculation methods for η. In this report, we used relatively low loading of Co-Pi films (~250 nanomoles Co), resulting in a lower activity and an impedance mismatch between the power supplied by the photovoltaic and the power utilized to drive the electrochemical half reaction. Improvements in efficiency per Eq. **2** are expected for deposition of thicker catalyst films, because the activity of the Co-Pi film has been shown to increase monotonically with catalyst loading on a planar electrode (3, 11). We have previously shown that it is possible to increase anode activity to 100 mA/cm^2 with a 3D catalyst support (11). Thus thicker Co-Pi films or thin Co-Pi films on a roughened (i.e., high surface area) Si surface will be better matched to the typical current densities obtained from crystalline Si solar cells at their maximum power point (~35 mA/cm^2) (44).

The Co-Pi-functionalized Si photoanode presented here embodies a promising approach for photovoltaic-photoelectrochemical water splitting that relies on operation at or near neutral pH. Photoelectrochemical water splitting (50) using single-junction concepts based on single-photon absorption have been widely investigated subsequent to the initial report by Fujishima and Honda of water splitting on TiO_2 photoelectrodes (51). The drawback of the single-photon approach is the requirement of large bandgap materials (which absorb only a small fraction of solar light) to generate sufficient photovoltage for water splitting. As a result, the maximum achievable solar-to-hydrogen efficiency is limited to ~7% for single-photon water splitting (27, 42). Multiphoton photoelectrochemical water splitting is more promising because higher efficiencies may be achieved (27, 42). In a multiphoton device architecture, the required potential for water oxidation is generated by sequential absorption of low-energy photons in a tandem solar cell. The most efficient photoelectrochemical tandem device for water splitting reported to date is 16.5% (hydrogen production efficiency) (52, 53). This device comprises a $GaInP_2$/GaAs tandem cell and platinum catalysts to produce hydrogen and oxygen, immersed in a strongly basic electrolyte (53). Although highly efficient, high costs are associated with the $GaInP_2$/GaAs tandem cell and the catalysts and device stability is poor (52). Though less efficient (2.5–8% hydrogen production efficiency), Si-based tandem cell concepts (33, 53–56) have promise of lower cost. These tandem cells typically consist of a stack of amorphous Si and Si-Ge alloys that are operated in basic electrolyte (pH > 13). The *p*-side of these tandem cells is usually passivated with ITO, which cannot be annealed because high-temperature treatment is detrimental to the amorphous Si in the tandem cell. Accordingly, the ITO offers only marginal protection of the Si from the extreme conditions of a caustic solution (36), thus resulting in decreased overall device performance (33). Higher efficiencies (up to 7.8%) (33, 53, 54) have been reported for tandem amorphous Si cells in which the oxygen evolving catalyst was not directly deposited on the solar cell, but connected to it through wires. The complexity of the fabrication of the latter PV-PEC devices however presents challenges for large-scale utilization. To this end, the Co-Pi-functionalized Si photoanode presented here provides distinct advantages because it can be operated under benign conditions. At pH = 7, a wide range of materials may be employed as a protective barrier layer of Si materials such as Fluorine-doped Tin Oxide (FTO) and ITO, which exhibit much better long-term stability at neutral pH relative to strongly acidic or alkaline conditions (57, 58). Moreover, the use of crystalline Si gives latitude in sample processing at higher temperatures; namely ITO can be annealed at temperatures approaching 400 °C to furnish a robust barrier layer, especially in a near-neutral pH electrolyte environment. The envisioned approach to connect three crystalline Si cells in series affords flexibility in achieving impedance matching as compared to a tandem cell concept, in which impedance matching has to be realized between the electrochemical load and the photovoltaic element and between the three light-absorbing elements within the solar cell. In the "series approach," impedance matching is only required between the photovoltaic element and the electrochemical load.

In conclusion, we demonstrated the successful integration of the water-splitting Co-Pi catalyst with a crystalline Si solar cell. That most of the voltage of the solar cell can be utilized to lower the onset potential for oxidation is a promising result. The device presented here serves as a proof of principle that photoelectrochemical water splitting may be achieved with crystalline Si photovoltaics and inexpensive catalysts at neutral pH, thus pointing the way to the development of inexpensive integrated devices for the *direct* solar-to-fuel conversion based on water splitting.

Materials and Methods

Boron-doped *p*-type silicon was used as a starting material and *np*-Si junction was created by phosphorous diffusion. The metallic contacts and the passivating layers were deposited on the *np*-Si wafer by sputtering methods. Details of the sample fabrication are provided in *SI Appendix*. Standard electrochemical techniques were used to electrodeposit the Co-Pi on Si-junction cells. The current-voltage (Tafel) behavior of the Co-Pi catalyst deposited on silicon in the region of water oxidation was measured over a 200 mV range in 10–30 mV increments. Because the onset potential for water oxidation is a function of the illumination intensity (Fig. 4*A*), the Tafel plot shows the potential (corrected for the solution resistance) vs. the log of the current

density. This approach is justified because we are primarily interested in Tafel slope, which does not change when using the absolute potential instead of the overpotential. Photoelectrochemistry measurements were done in a one-compartment cell with a flat fused silica surface; the light source was a Xe lamp equipped with a filter to modify the spectral distribution of the Xe lamp in order to match the solar spectrum. Faradaic efficiencies were measured fluorescence-based O_2 sensor techniques. More detailed descriptions of the electrochemical methods employed in these studies, IPCE, and other photoelectrochemical measurement methods are provided as *SI Appendix*. In addition, the *SI Appendix* provides additional data for CVs, Current-Voltage (IV) curves of solar cells, absorption spectra, and a comparison between two methods for calculating conversion efficiencies.

ACKNOWLEDGMENTS. We thank Kurt Broderick of the MIT Microelectronics Technology Laboratory for help with thin film processing. We also acknowledge Rupak Chakraborty for help with the IPCE measurements. This work is part of the research program "Fellowships for Young Energy Scientists" (YES!) of the Foundation for Fundamental Research on Matter (FOM), which is financially supported by the Netherlands Organization for Scientific Research (NWO). NWO is also gratefully acknowledged for supplying a Rubicon grant (to J.J.H.P.) Y.S. gratefully acknowledges the National Science Foundation (NSF) for a predoctoral fellowship. D.G.N. acknowledges support with grants from the NSF CHE-0533150 and from the Air Force Office of Scientific Research (AFOSR) FA9550-09-1-0689, and he thanks the Chesonis Family Foundation for their support. T.B. also acknowledges support from the Chesonis Family Foundation.

1. Barber J (2007) Biological solar energy. *Philos T Roy Soc A* 365:1007–1023.
2. Betley TA, Wu Q, Van Voorhis T, Nocera DG (2008) Electronic design criteria for O-O bond formation via metal-oxo complexes. *Inorg Chem* 47:1849–1861.
3. Surendranath Y, Kanan MW, Nocera DG (2010) Mechanistic studies of the oxygen evolution reaction by a cobalt-phosphate catalyst at neutral pH. *J Am Chem Soc* 132:16501–16509.
4. Kanan MW, Nocera DG (2008) In situ formation of an oxygen-evolving catalyst in neutral water containing phosphate and Co^{2+}. *Science* 321:1072–1075.
5. Dincă M, Surendranath Y, Nocera DG (2010) A nickel-borate oxygen evolving catalyst that functions under benign conditions. *Proc Natl Acad Sci USA* 107:10337–10341.
6. Kanan MW, Surendranath Y, Nocera DG (2009) Cobalt-phosphate oxygen-evolving compound. *Chem Soc Rev* 38:109–114.
7. Ono T (2001) Metallo-radical hypothesis for photoassembly of $(Mn)_4$-cluster of photosynthetic oxygen evolving complex. *Biochim Biophys Acta* 1503:40–51.
8. Burnap RL (2004) D1 protein processing and Mn cluster assembly in light of the emerging Photosystem II structure. *Phys Chem Chem Phys* 6:4803–4809.
9. Ananyev GM, Zaltsman L, Vasko C, Dismukes GC (2001) The inorganic biochemistry of photosynthetic oxygen evolution/water oxidation. *Biochim Biophys Acta* 1503:52–68.
10. Surendranath Y, Dincă M, Nocera DG (2009) Electrolyte-dependent electrosynthesis and activity of cobalt based water oxidation catalysts. *J Am Chem Soc* 131:2615–2620.
11. Esswein AJ, Surendranath Y, Reece SR, Nocera DG (2011) Highly active cobalt phosphate and borate based oxygen evolving anodes operating in neutral and natural waters. *Energ Environ Sci* 4:499–504.
12. Huynh MHV, Meyer TJ (2007) Proton-coupled electron transfer. *Chem Rev* 107:5004–5064.
13. Siegbahn PEM (2009) An energetic comparison of different models for the oxygen evolving complex of photosystem II. *J Am Chem Soc* 131:18238–18239.
14. Lutterman DA, Surendranath Y, Nocera DG (2009) A self-healing oxygen-evolving catalyst. *J Am Chem Soc* 131:3838–3839.
15. Prásil O, Adir N, Ohad I (1992) Dynamics of photosystem II: Mechanism of photoinhibition and recovery process. *The Photosystems: Structure, Function and Molecular Biology*, ed J Barber (Elsevier Science Publishers, Amsterdam, The Netherlands), 11, pp 295–348.
16. Aro EM, Virgin I, Andersson B (1993) Photoinhibition of photosystem II—inactivation, protein damage and turnover. *Biochim Biophys Acta* 1143:113–134.
17. Andersson B, Aro EM (2001) Photodamage and D1 protein turnover in photosystem II. *Regulation of Photosynthesis*, eds EM Aro and B Anderson (Kluwer Academic, Dordrecht, The Netherlands), pp 377–393.
18. Barber J, Andersson B (1992) Too much of a good thing: light can be bad for photosynthesis. *Trends Biochem Sci* 17:61–66.
19. Risch M, et al. (2009) Cobalt-oxo core of a water-oxidizing catalyst film. *J Am Chem Soc* 131:6936–6937.
20. Kanan MW, et al. (2010) Structure and valency of a cobalt-phosphate water oxidation catalyst determined by in situ X-ray spectroscopy. *J Am Chem Soc* 132:13692–13701.
21. Barber J (2008) Crystal structure of the oxygen-evolving complex of photosystem II. *Inorg Chem* 47:1700–1710.
22. Zhong DK, Sun J, Inumaru H, Gamelin DR (2009) Solar water oxidation by composite catalyst/α-Fe_2O_3 photoanodes. *J Am Chem Soc* 131:6086–6087.
23. Zhong DK, Gamelin DR (2010) Photoelectrochemical water oxidation by cobalt catalyst ("Co-Pi")/α-Fe_2O_3 composite photoanodes: oxygen evolution and resolution of a kinetic bottleneck. *J Am Chem Soc* 132:4202–4207.
24. Zhong DK, Cornuz M, Sivula K, Grätzel M, Gamelin DR (2011) Photo-assisted electrodeposition of cobalt-phosphate (Co-Pi) catalyst on hematite photoanodes for solar water oxidation. *Energ Environ Sci*, Advance Article DOI: 10.1039/C1EE01034D.
25. Seabold JA, Choi KS (2011) Effect of a cobalt-based oxygen evolution catalyst on the stability and the selectivity of photo-oxidation reaction of a WO_3 photoanode. *Chem Mater*, DOI: 10.1021/cm1019469.
26. Steinmiller EMP, Choi KS (2009) Photochemical deposition of cobalt-based oxygen evolving catalyst on a semiconductor photoanode for solar oxygen production. *Proc Natl Acad Sci USA* 106:20633–20636.
27. Weber MF, Dignam MJ (1986) Splitting water with semiconducting photoelectrodes - efficiency considerations. *Int J Hydrogen Energ* 11:225–232.
28. Lewis NS, Nocera DG (2006) Powering the planet: chemical challenges in solar energy utilization. *Proc Natl Acad Sci USA* 103:15729–15735.
29. Nocera DG (2010) Fast food energy. *Energ Environ Sci* 3:993–995.
30. Cook TR, et al. (2010) Solar energy supply and storage for the legacy and non-legacy world. *Chem Rev* 110:6474–6502.
31. Nocera DG (2009) Personalized energy: the home as a solar power station and solar gas station. *ChemSusChem* 2:387–390.
32. Zhang XG (2001) *Silicon and its Oxide* (Kluwer Academic Publishers, New York).
33. Kelly NA, Gibson TL (2006) Design and characterization of a robust photoelectrochemical device to generate hydrogen using solar water splitting. *Int J Hydrogen Energ* 31:1658–1673.
34. Narasimha S, Rohatgi A, Weeber AW (1999) An optimized rapid aluminum back surface field technique for silicon solar cells. *IEEE Transactions on Electron Devices* 46:1363–1370.
35. Hodes G, Thompson L, DuBow J, Rajeshwar K (1983) Heterojunction silicon/indium tin oxide photoelectrodes: development of stable systems in aqueous electrolytes and their applicability to solar energy conversion and storage. *J Am Chem Soc* 105:324–330.
36. Hennig H, Heckner KH, Hirsch D, Ladwig H (1982) The influence of the preparation on layer properties of transparent indium-tin oxide electrodes. *Phys Status Solidi A* 74:133–139.
37. Park Y, Choong V, Gao Y, Hsieh BR, Tang CW (1996) Work function of indium tin oxide transparent conductor measured by photoelectron spectroscopy. *Appl Phys Lett* 68:2699–2701.
38. Ho JJ, Chen CY, Hsiao RY, Ho OL (2007) The work function improvement on indium-tin-oxide epitaxial layers by doping treatment for organic light-emitting device applications. *J Phys Chem C* 111:8372–8376.
39. Novikov A (2010) Experimental measurement of work function in doped silicon surfaces. *Solid State Electron* 54:8–13.
40. McAlpin JG, et al. (2010) EPR evidence for Co(IV) species produced during water oxidation at neutral pH. *J Am Chem Soc* 132:6882–6883.
41. Symes MD, Surendranath Y, Lutterman DA, Nocera DG (2011) Bidirectional and unidirectional PCET in a molecular model of a cobalt-based oxygen evolving catalyst. *J Am Chem Soc* 133:5174–5177.
42. Rocheleau RE, Miller EL (1997) Photoelectrochemical production of hydrogen: engineering loss analysis. *Int J Hydrogen Energ* 22:771–782.
43. Surendranath Y, Nocera DG (2011) Oxygen evolution reaction chemistry of oxide-based electrodes. *Prog Inorg Chem*, in press.
44. Nelson J (2003) *The Physics of Solar Cells* (Imperial College Press, London).
45. Folcher G, Cachet H, Froment M, Bruneaux J (1997) Anodic corrosion of indium tin oxide films induced by the electrochemical oxidation of chlorides. *Thin Solid Films* 301:242–248.
46. Matveeva E (2005) Electrochemistry of the indium-tin oxide electrode in 1 M NaOH electrolyte. *J Electrochem Soc* 152:H138–H145.
47. Yang JC (1998) Advances in amorphous silicon alloy technology—the achievement of high-efficiency multijunction solar cells and modules. *Prog Photovoltaics* 6:181–186.
48. Rech B, Wagner H (1999) Potential of amorphous silicon for solar cells. *Appl Phys A-Mater* 69:155–167.
49. Parkinson B (1984) On the efficiency and stability of photoelectrochemical devices. *Acc Chem Res* 17:431–437.
50. Walter MG, et al. (2010) Solar water splitting cells. *Chem Rev* 110:6446–6473.
51. Fujishima A, Honda K (1972) Electrochemical photolysis of water at a semiconductor electrode. *Nature* 238:37–38.
52. Khaselev O, Turner JA (1998) A monolithic photovoltaic-photoelectrochemical device for hydrogen production via water splitting. *Science* 280:425–427.
53. Khaselev O, Bansal A, Turner JA (2001) High-efficiency integrated multijunction photovoltaic/electrolysis systems for hydrogen production. *Int J Hydrogen Energ* 26:127–132.
54. Rocheleau RE, Miller EL, Misra A (1998) High-efficiency photoelectrochemical hydrogen production using multijunction amorphous silicon photoelectrodes. *Energy and Fuels* 12:3–10.
55. Yamane S, et al. (2009) Efficient solar water splitting with a composite n-Si/p-CuI/n-i-p a-Si/n-p GaP/RuO_2 semiconductor electrode. *J Phys Chem C* 113:14575–14581.
56. Yamada Y, et al. (2003) One chip photovoltaic water electrolysis device. *Int J Hydrogen Energ* 28:1167–1169.
57. Kraft A, Hennig H, Herbst A, Heckner KH (1994) Changes in electrochemical and photoelectrochemical properties of tin-doped indium oxide layers after strong anodic polarization. *J Electroanal Chem* 365:191–196.
58. Wang X, Zhi L, Mullen K (2007) Transparent, conductive graphene electrodes for dye-sensitized solar cells. *Nano Lett* 8:323–327.